

physica **p** status **s** solidi **s**

www.pss-journals.com

reprint



Simulations of photocurrent improvement through combined geometric/diffracting light trapping in organic small molecule solar cells

Marcos Soldera*, Emiliano Estrada, and Kurt Taretto

Departamento de Electrotecnia, Universidad Nacional del Comahue – CONICET, Buenos Aires 1400, 8300 Neuquen, Argentina

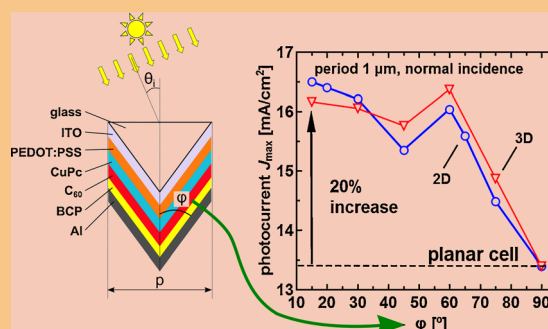
Received 19 September 2012, revised 20 March 2013, accepted 22 March 2013

Published online 18 April 2013

Keywords finite element method, light trapping, organic solar cells

* Corresponding author: e-mail marcos.soldera@fain.uncoma.edu.ar, Phone/Fax: +54 299 4488305

Although organic solar cells have recently shown remarkable high power conversion efficiencies approaching 12%, further improvements are needed to become a low cost alternative to current inorganic photovoltaic technologies. Optical losses due to insufficient light trapping, parasitic absorption in the contact layers and reflectance limit drastically the photocurrent delivered by these solar cells. In this work, we simulated two- (2D) and three-dimensional (3D) surface textures in the micro- and submicroscale to improve light trapping in optimized organic solar cells based on copper phthalocyanine (CuPc) and fullerene (C₆₀). The analysis was carried out with the aid of the finite element method in 2D and 3D, taking into account interference as well as reflection and diffraction of the incident AM1.5 spectrum. At normal incidence, up to 23% improvement in the photocurrent over the planar cell was obtained. To investigate the texture performance under practical circumstances, we simulated 2D microstructures during a typical summer day, taking the change of incidence angle and radiation intensity into account. Results clearly show that all textured cells deliver more photocurrent than the planar cell, even at oblique angles.



The left illustration shows the simulation setup of the 2D geometry detailing the materials and simulation parameters. The right plot shows the calculated photocurrent improvement for 2D V-grooved cells and for 3D pyramid-shaped cells at normal incidence as a function of the aperture angle ϕ .

© 2013 WILEY-VCH Verlag GmbH & Co. KGaA, Weinheim

1 Introduction With a confirmed power conversion efficiency of 11% [1], organic solar cells are proving their potential to become a low-cost alternative to inorganic photovoltaics. The expectation of low-cost organic photovoltaics relies on the ease of manufacture based on roll-to-roll processing without the need of clean room facilities [2, 3]. However, efficiencies approaching 10% are still three times lower than the radiative efficiency limit of these materials systems [4]. Among the several causes of this mismatch between theory and state-of-the-art cells, we

focus on the optical losses due to insufficient light trapping, reflectance, and parasitic absorption in the contact layers.

In order to efficiently collect photogenerated carriers, organic semiconductor layers must be deposited with thicknesses comparable to the exciton diffusion length, which lies typically in the range of 10–60 nm [5, 6]. However, these thicknesses are an order of magnitude lower than typical absorption lengths, resulting in incomplete light absorption especially in the red-infrared portion of the solar spectrum. In inorganic solar cells, such weak light absorption

has been mitigated through different approaches, efficiently reducing this optical loss [7–10]. Among these techniques, geometric light trapping is already well-established in thin film crystalline and amorphous Si solar cells [11–15] and consists in texturizing the front or back cell surface profiting from two fundamental phenomena. On the one hand, the optical path inside the cell is extended by allowing the radiation enter the cell at an oblique angle [16, 17], and on the other hand, light is trapped by internal reflection and therefore the incoming rays can bounce between the facets several times before they reflect back [18].

Surface texturing in the microscale can be achieved by several methods such as wet-chemical etching [19], optical lithography [20], nanoimprint lithography [21], ion beam lithography [22], and direct laser interference patterning (DLIP) [23]. The latter is based on the formation of an interference pattern produced by two or more coherent laser beams on an absorber material. One- and two-dimensional (2D) periodic patterns with periods extending from hundreds of nanometers up to several micrometers are then obtained by direct ablation of the sample. This technique can be scalable to industrial standards since it is a single step process which does not require masks, templates, or solvents and can provide relatively fast fabrication rates [24–26]. It was recently reported an enhancement in power conversion efficiency for organic solar cells through surface texturing using DLIP [27]. A conformal zinc phthalocyanine (ZnPc) and fullerene (C_{60}) film was deposited by vacuum thermal evaporation (VTE) onto laser patterned polyethylene terephthalate (PET) with hexagonal grid structure of $0.7\ \mu\text{m}$ period. The short circuit current density was reported to be 18% higher than the planar cell, resulting from the enhanced absorption in the semiconductor layer.

We notice that the compatibility between the deposition technique for the active layers and the structured substrate geometry deserves special attention. For instance, although VTE is commonly used for depositing small molecule materials, it may be inefficient for preparing conformal films on small aperture angles and textures in the μm -scale. Evaporated molecules under high vacuum follow ballistic trajectories, resulting in non-uniform thicknesses of the semiconductor layers [28]. In contrast, the organic vapor phase deposition (OVPD) [29] technique uses a background transport gas, producing a disordered flux of the evaporated molecules toward the substrate. We therefore suggest that OVPD may be suitable to deposit conformal organic films onto most of the textures studied here.

Optical modeling is a powerful tool to recognize the loss factors that limit the light absorption in the active layers. In addition, it can be used to optimize geometries and architectures before their implementation. Numerical modeling through ray tracing, finite element, and finite difference time domain methods have been extensively used to understand and optimize photon management in textured inorganic and organic thin film solar cells [30–33].

In this contribution, we investigate the potential improvement in photocurrent upon implementing light

trapping geometries in organic solar cells based on the material system CuPc/ C_{60} , which is a reference heterojunction among the small molecular weight semiconductors. We simulate the maximum photocurrent delivered by V-grooved (2D) and pyramid-textured [three-dimensional (3D)] solar cells with the finite element method in 2D and 3D, taking into account interference as well as reflection, and diffraction of the incident AM1.5 spectrum. We also simulate V-grooves during a typical summer day to evaluate their performance under a more realistic environment, where solar radiation impinges at different angles during daylight. In addition, we discuss whether inhomogeneous illumination caused by illumination at oblique angles affects the power conversion efficiency of the structured cells.

The paper is organized as follows, in Section 2 we describe the simulation model and the simplifications assumed to obtain the photocurrent in each geometry. Next, in Section 3.1 we present and discuss the results for all the geometries modeled at normal incidence, explaining the roles of reflection and diffraction. Then, in Section 3.2 we show the results for the full day simulations and discuss the overall performance of structured cells during a whole day. Finally, in Section 4 we draw the conclusions of this work.

2 Modeling

2.1 Geometry and meshing We took as a starting point for our simulations the optimized planar cell reported in Ref. [34], which consisted of six layers stacked above a glass superstrate according to the following sequence: a transparent indium-tin oxide (ITO) front contact, a poly(3,4-ethylenedioxythiophene):poly(styrenesulfonate) (PEDOT:PSS) electron barrier, the optical active layers copper phthalocyanine (CuPc) as the hole conducting material and fullerene (C_{60}) as the electron conducting material, then a bathocuproine (BCP) hole barrier and finally Al as back contact and reflector. All materials in this work were considered linear, homogeneous, and isotropic, and their optical parameters were obtained from the literature [35–37]. Figure 1a shows the modeled V-groove geometry, while Fig. 1b displays the simulated square-based pyramid. The simulations were aimed at finding optimum texture parameters relevant to fabrication processes. Therefore, we use the aperture angle φ and period p as simulation parameters as shown in Fig. 1a. We let p vary from 0.5 to $10\ \mu\text{m}$ and φ from 15° to 90° , the latter corresponds to the planar cell. The combination of these parameters yield geometries that are feasible to achieve with the current DLIP technology. The layer thicknesses used in the simulations were also taken from the optimized cell of Ref. [34] and are detailed in Fig. 1a.

The finite element method was implemented with the software *COMSOL Multiphysics 3.5a* [38]. Since we are interested in finding the steady state solutions, Maxwell's equations were solved assuming that all variations in time can be expressed as sinusoidal signals, which case is

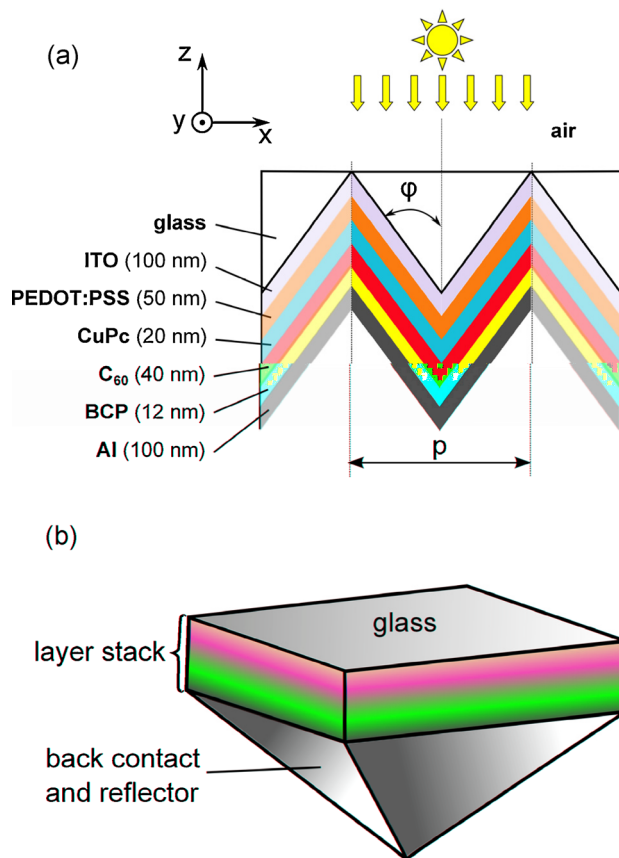


Figure 1 Schematic illustration of the simulated (a) V-groove and (b) pyramid. Materials, thicknesses and simulation parameters common to both geometries are specified in (a).

known as time harmonic propagation [39]. The formulation of this problem setting the wavelength as predefined variable yielded complex valued solutions, which represent the amplitude and phase of the electromagnetic field.

The mesh was generated by COMSOL using triangular/tetrahedral elements for the 2D/3D simulations with the constraint that the minimum effective wavelength exceeds at least five times the element size in each subdomain [39]. With this consideration, typical mesh sizes ranged from 10 000 to 100 000 elements for the 2D geometries, and from 100 000 to 180 000 for the 3D cases.

The incident radiation corresponds to the solar AM1.5G 100 mW cm⁻² spectrum in the wavelength range 300–800 nm with a resolution of 5 nm, entering from an inner virtual boundary into the air domain toward the cell surface. This boundary permits all the waves reflected at the cell surface to be transmitted into a perfectly matched layer (PML), where the waves become completely damped, avoiding subsequent re-entering of reflected light [40]. We took advantage of the twofold symmetry of the 2D grooves by simulating half-grooves, and thus reducing the mesh size by a factor 2. To account for the mainly non-polarized solar radiation [41], we allowed for s- and p-polarized light, *i.e.*,

electric field perpendicular and parallel to the x - z plane, respectively, and averaged the photocurrent delivered by both polarizations. Analogously, we profited from the fourfold symmetry of the 3D pyramids by simulating quarter-pyramids and single electric field polarization in the x - y plane, which reduced drastically the computation time. The lateral boundary conditions (LBC) were set as follows. In the 2D simulations, the LBC must account for the superposition of the reflected waves from both facets at the axis of the V-groove, which corresponds to the left LBC in our half-grooves. Along this axis, the reflected waves electric/magnetic z -components, for the p-/s-polarization, respectively, interfere destructively, and therefore the resulting electric/magnetic field is perpendicular to the groove axis. Likewise, the right LBC is forced according to this restriction. This strategy applies to the 3D simulations as well, and thus we set the LBC at opposite faces pair-wise forcing the electric and magnetic fields to be perpendicular to the pyramid axis.

We simplified the complexity of establishing LBC to the oblique incidence at the V-grooves by simulating three adjacent identical cells and analyzing the absorbance in the middle one. Then, enclosing the geometry with PML's at both sides allowed us to disregard the LBC. The incident spectrum corresponds to the AM1.5G with its power density modulated according to the solar time during a clear summer day at a latitude of 40° south. We aligned the grooves in the south–north direction and considered that the cells are tilted north at an angle of 40°. Although the geometry of the problem is intrinsically 3D, we reduced the model to a 2D problem projecting the incidence angle onto the plane of the solar cells. We followed the mathematical approach given in Ref. [41] to obtain the Sun's position and intensity according to these conditions.

2.2 Electromagnetic model The average energy absorption of a plane electromagnetic wave with wavelength λ in a material with complex index of refraction $\tilde{n}(\lambda) = n(\lambda) + ik(\lambda)$ reads [42]

$$Q(x, y, z, \lambda) = \frac{1}{2} c \varepsilon_0 n(\lambda) \alpha(\lambda) |E(x, y, z, \lambda)|^2, \quad (1)$$

where E is the electric field, (x, y, z) are the spatial coordinates, c the speed of light in vacuum, ε_0 the permittivity of free space, and α is the absorption coefficient defined as $\alpha = 4\pi k(\lambda)/\lambda$. Here, Q is given per unit time and volume, meaning a specific power absorption.

We assumed that in the active layers an exciton is created per each absorbed photon, implying that the exciton generation rate is defined as the quotient between the absorbed energy and the incident photon energy as $G_\lambda(x, y, z, \lambda) = Q(x, y, z, \lambda)/(hc/\lambda)$, where h is Planck's constant. Next, assuming that excitons dissociate into free carriers with perfect efficiency, we are able to set the free carrier generation rate G as $G = G_\lambda$. Finally, if every free carrier is extracted through the contacts of the solar cell,

the maximum photocurrent density will be given by the volume integral

$$J_{\max} = q \int GdV/A, \quad (2)$$

where q is the elementary charge and A is the projected cell area in the x - y plane. For the 3D simulations it holds that $A = p^2$, while for the 2D simulations it must hold that $A = p \times 1 \text{ m}$, so that A is consistent with surface units.

3 Results and discussion

3.1 Normal incidence First we simulated the planar cell ($\varphi = 90^\circ$), obtaining a maximum photocurrent $J_{\max} = 13.4 \text{ mA cm}^{-2}$, which is 7% higher than the short circuit current density $J_{\text{sc}} = 12.5 \text{ mA cm}^{-2}$ determined from experimental data reported by Ref. [34]. This difference arises from exciton and free carrier collection losses which are not taken into account by our model.

Figure 2a shows the maximum photocurrent J_{\max} as a function of the aperture angle φ with the period p as a parameter for the 2D (open symbols) and 3D (triangles) simulations. According to geometric optics, the maximum number of consecutive bounces a ray incoming at an incidence angle θ_i suffers between facets is given by [43]

$$N_{\max} = (180^\circ - \theta_i + \varphi)/2\varphi, \quad (3)$$

and is plotted as a function of φ in Fig. 2b for normal incidence. We observe that the photocurrents delivered by the 2D and 3D textures show similar trends, and in all cases they provide more photocurrent density than the planar cell. However, J_{\max} does not grow monotonously as the

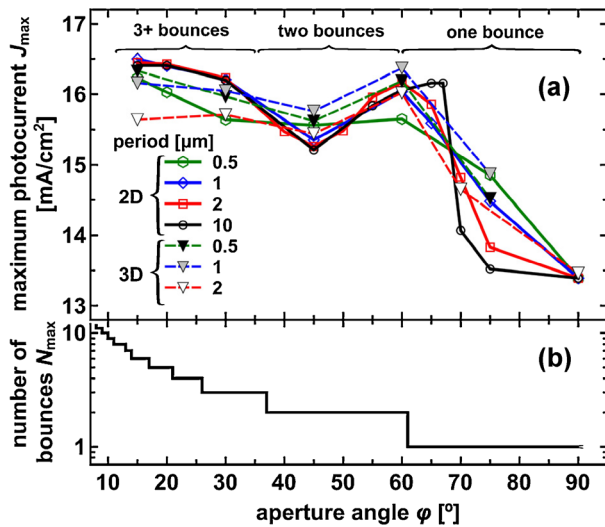


Figure 2 (a) Maximum photocurrent J_{\max} as a function of the texture aperture angle φ delivered by 2D V-grooved cells (open symbols) and by the 3D pyramid textured cells (triangles). All the structured cells provide more photocurrent than the planar device ($\varphi = 90^\circ$). (b) Maximum number of bounces between facets N_{\max} an incoming ray suffers according to geometric optics. Three regimes are identified according to N_{\max} .

dependence of N_{\max} with φ would suggest. In order to gain a deeper insight into this behavior, we divided the plot into three regimes, according to the number of consecutive bounces the rays undergo between facets (see Fig. 2a).

The first regime ($60^\circ < \varphi < 90^\circ$) belongs to the case in which the incident wave strikes the facets only once ($N_{\max} = 1$). The fraction that reflects at the glass/ITO interface, or at any other interface within the cell, propagates toward the glass/air interface at an oblique angle. As φ decreases, the reflected rays hit the glass/air interface at increasing angles with respect to the normal, enhancing the internal reflectance at this interface according to Fresnel's coefficients [44], and ultimately leading to the increase in J_{\max} relative to the planar cell. The steep increase of J_{\max} around $\varphi \cong 68^\circ$ corresponds to the onset of total internal reflection at the glass/air interface, resulting from the incidence at angles larger than the glass-to-air critical angle $\theta_c \cong 42^\circ$. Turning to the dependence on the texture period p , we observe in this regime an overall increase in J_{\max} with smaller values of p . We attribute this dependence to diffraction of incoming light at the periodic pattern as p approaches the wavelength in glass for the visible portion of the solar spectrum. In the following, we explain qualitatively this effect assuming that the structured cells with $\varphi > 70^\circ$ work as line gratings with a grating constant p . Under normal incidence, the diffracted beams travel toward the glass/air interface following the directions θ_m given by the expression $\sin(\theta_m) = m\lambda/pn_{\text{glass}}$, where m is the diffraction order and $n_{\text{glass}} \cong 1.46$ is the index of refraction of glass.

In order to investigate the influence of p on the direction of diffracted modes, we plotted in Fig. 3 the first-order diffracted angle θ_1 as a function of p . The inset in Fig. 3 outlines an incident beam which diffracts at the periodic structure and splits into two modes following the directions

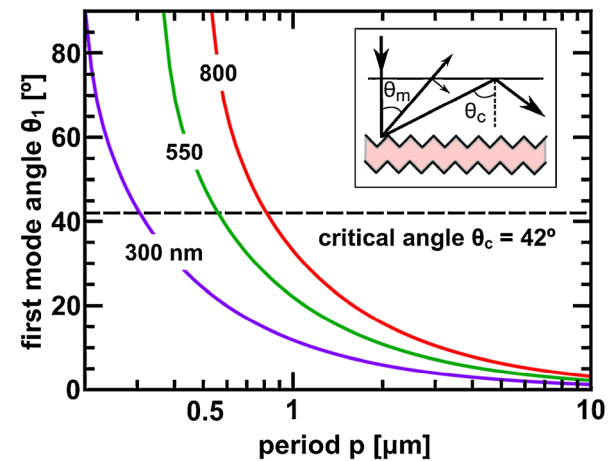


Figure 3 First-order diffracted angle θ_1 for incoming light interacting with structured cells with period p for three wavelengths. At periods $p < 1 \mu\text{m}$, the diffracted beams hit the glass/air interface at angles above the critical angle for the red-infrared spectrum, and therefore total internal reflection takes place as shown in the inset.

given by θ_m . One of the modes is partially reflected at the glass/air interface, whereas the other suffers total internal reflection, contributing to the absorption to a larger degree. Figure 3 shows that at p much higher than λ , θ_1 tends to zero, which means that the diffracted beam is almost parallel to the zero-order beam, and thus diffraction is negligible. For shorter grating constants, the first order diffracted beam increases rapidly. For instance, at $p < 1 \mu\text{m}$, the first-order diffracted beam strikes the glass/air interface at angles $\theta_1 > \theta_c$ for wavelengths in the red-infrared spectrum. This diffractive effect traps light efficiently, explaining the increase of J_{max} as p decreases as seen in Fig. 2a, first regime.

The second regime corresponds to the range $36^\circ < \varphi \leq 60^\circ$, where $N_{\text{max}} = 2$. The large photocurrent around $\varphi = 60^\circ$ seen in Fig. 2a is attributed to an increase in absorption due to the second bounce of incoming rays, and to the grazing incidence of reflected beams at the glass/air interface, which reduces the transmittance into the air. As the aperture angle decreases, the second reflected beam hits the glass/air interface at smaller angles, and therefore the transmitted fraction of this beam to the air increases. In the singular case of $\varphi = 45^\circ$, two consecutive reflections between facets drives the reflected beam toward the glass/air interface at a perpendicular angle, and thus the transmittance into the air is maximum. This effect is noticed by the dip in J_{max} at $\varphi = 45^\circ$ as seen in Fig. 2a. In the range $36^\circ < \varphi < 45^\circ$ the reflected beams hit the glass/air interface at oblique incidence, and thus J_{max} increases again.

In the third regime ($\varphi \leq 36^\circ$) we obtained the maximum value of the photocurrent among all the simulated geometries of $J_{\text{max}} = 16.5 \text{ mA cm}^{-2}$ at a V-grooved textured with $p = 1 \mu\text{m}$ and $\varphi = 15^\circ$, which is 23% higher than photocurrent delivered by the planar cell. We observe that overall J_{max} reaches its maximum at $\varphi = 15^\circ$ for each simulated geometry. Analyzing the spectral absorbance and reflectance of cells with different aperture angles, we find that parasitic absorbance plays an important role in the third regime. For instance, we show for comparison the absorbance distribution of the planar cell (Fig. 4a) and the V-grooved cell with $\varphi = 15^\circ$ and $p = 1 \mu\text{m}$ (Fig. 4b). Naturally, the increase in absorption in the active layers explains the increase in the maximum photocurrent of the structured cell relative to the planar device. However, parasitic absorption increases as well, especially in the ITO and PEDOT:PSS layers, due to the lengthening of the light path. Quantitatively the integral absorbance of the active layers improves from 53.7% in the planar cell to 63.2% in the V-grooved cell with $\varphi = 15^\circ$ and $p = 1 \mu\text{m}$, while the parasitic absorbance increases from 18.9 to 33.3%, respectively. As a consequence, the reflectance becomes drastically reduced from an integral value of 27.4 to 3.5%, respectively. We found that 10% of solar radiation within the wavelength range from 350 to 750 nm is absorbed in the anode for the structured cells with $\varphi = 15^\circ$. On the other hand, this result suggests an additional improvement potential of up to 10% in the photocurrent, if novel transparent front contacts with increased transmittance in the visible spectrum are devel-

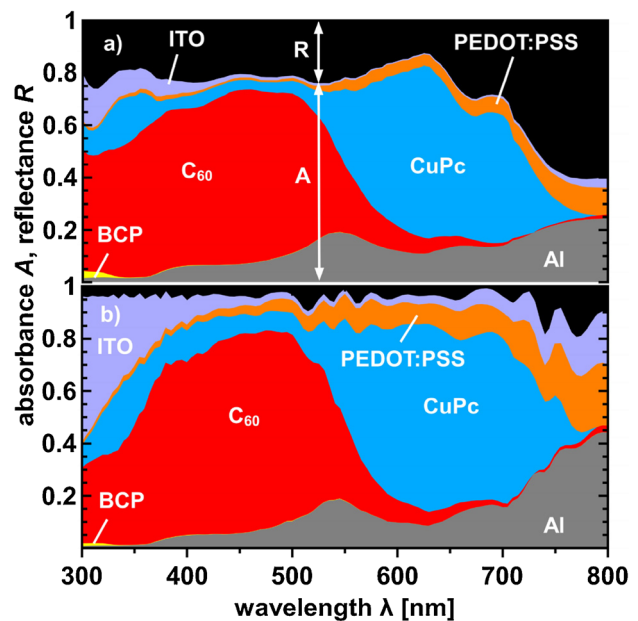


Figure 4 Spectral reflectance and absorbance obtained for each layer for (a) the planar cell and (b) folded cell with aperture angle $\varphi = 15^\circ$ and period $p = 1 \mu\text{m}$. The increase in the absorbance in the active layer (C_{60} and CuPc) correlates with the enhancement in the photocurrent in the textured cell. However, parasitic absorbance in the remaining layers, especially in the anode layers, increases as well.

oped. In this regime, we observe a very weak dependence of the maximum photocurrent at low φ on the period as long as it holds that $p \geq 1 \mu\text{m}$.

The general trend shows that at normal incidence the textures with the smallest aperture angle $\varphi = 15^\circ$ yielded the highest photocurrent, in agreement with several studies on microtextured organic cells reported elsewhere [31, 45, 46].

3.2 Oblique incidence Figure 5 shows the photocurrent delivered by the V-grooved cells from noon, *i.e.*, normal incidence ($\theta_i = 0^\circ$), to sunset ($\theta_i \cong 80^\circ$) of a summer day as described in Section 2.1. The simulated cells have a fixed period $p = 2 \mu\text{m}$ and the aperture angle is used as a parameter. We also included the response of the planar cell for comparison (open circles). Notice that all structured cells deliver more photocurrent than the planar device during the whole day. The inset in Fig. 5 shows that the averaged photocurrent during the day decreases monotonically as the aperture angle increases.

Light impinging at oblique incidence illuminates directly only one facet, while the other becomes partially shaded. Although we observed an increase in the photocurrent of V-grooved cells compared to the planar device, the mismatch of illumination intensity on the facets gives rise to the question whether the actual power delivered by the structured cells is higher as well. To address this issue we analyze the performance of the structured and planar cells at an incidence angle $\theta_i = 50^\circ$ for a summer day. We define the

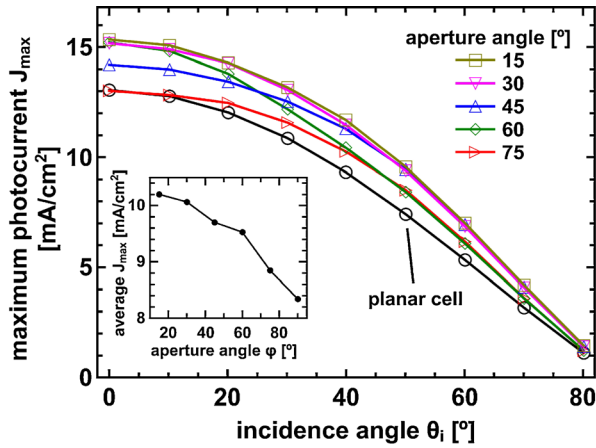


Figure 5 Maximum photocurrent J_{max} delivered by the planar and structured cells with period $p = 2 \mu\text{m}$ at oblique angles θ_i for a typical summer day (see Section 2.1 for simulation details). All the structured cells provide more photocurrent than the planar cell during the whole day. The inset shows the daily averaged photocurrent as a function of the aperture angle.

shadowing factor $f_{sh} = G_{\chi}^{il}/G_{\chi}^{sh}$, where $G_{\chi}^{il,sh}$ is the total exciton generation rate in the illuminated/shaded facet. Our simulations of V-grooved cells with $2 \mu\text{m}$ period and variable aperture angle show that the shadowing factor spans in the range $f_{sh} = 1.6\text{--}2.3$, which means that on average, at $\theta_i = 50^\circ$, the shaded facet deliver about half the current than the illuminated one. Some of the causes for this non-negligible exciton generation rate in the shaded facet are the change in propagation direction due to refraction of the incoming light at the air/glass interface [case (i) in Fig. 6], reflection of incoming rays at the first layer of the illuminated facet [case (ii) in Fig. 6] and reflection of weakly absorbed light occurring at the back layer of the illuminated facet [case (iii) in Fig. 6].

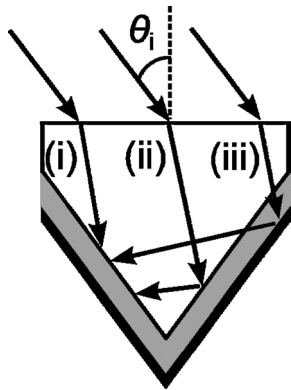


Figure 6 Schematic of a V-grooved cell under oblique incidence. The left facet is only partially shaded due to the following causes: (i) refraction, (ii) reflection at the anode layer at the illuminated facet, and (iii) reflection at the back reflector of the illuminated facet.

In order to estimate the power conversion efficiency of a partially shaded V-grooved cell, we model each facet as a single solar cell following the simple one-diode model for solar cells without resistive losses [47]. Figure 7 shows the equivalent electrical circuit of a partially shaded textured cell. The current density as a function of the applied bias V in the structured cell is given by

$$J(V) = 2 \times J_0 \left(e^{V/nV_t} - 1 \right) - J_{il} - J_{sh}, \quad (4)$$

where the factor 2 indicates that the dark current density of both facets are equal, then $J_{il,sh}$ are the photocurrents delivered by the illuminated and shaded facets, respectively, which are linked through the shadowing factor $f_{sh} = J_{il}/J_{sh}$. Then, J_0 is the saturation current density, n is the diode ideality factor, and V_t is the thermal voltage.

According to measurements reported in Ref. [48] for CuPc/C₆₀ based solar cells, we set the diode ideality factor $n = 2$. We applied the one-diode model for a planar cell under AM1.5G illumination, and set $J_0 = 2 \times 10^{-4} \text{ mA cm}^{-2}$ in order to obtain an open circuit voltage $V_{oc} = 0.58 \text{ V}$, which corresponds to the experimental values reported in Ref. [34]. In order to obtain the open circuit voltage V_{oc} and power conversion efficiency PCE of the textured cells using Eq. (4), we consider that the textured cell short circuit current J_{sc} equals the maximum photocurrent J_{max} at $\theta_i = 50^\circ$ shown in Fig. 5, namely $J_{max}(\theta_i = 50^\circ) = J_{sc} = J_{il} + J_{sh} = (1 + f_{sh}^{-1})J_{il}$. In Fig. 8 we plot J_{sc} , V_{oc} and PCE as a function of the aperture angle of the structured cells normalized to the values of the planar device. The variation of the shadowing factor f_{sh} (right axis) can be qualitatively understood considering ray optics as follows. Recalling Eq. (3), textures with small aperture angles trap light very efficiently due to multiple reflections between facets. Therefore, f_{sh} is low for $\varphi \leq 30^\circ$ due to the predominance of mechanisms (ii) and (iii) depicted in Fig. 6. When the aperture angle increases to $\varphi = 45^\circ$, the rays reflected at the illuminated facet hit the shaded facet at a very shallow angle, and therefore they are mostly redirected outwards and lost to the environment. As a consequence, light is hardly absorbed in the shaded facet and thus the shadowing factor is higher. According to Eq. (3), for $\varphi > 50^\circ$ multiple reflections are suppressed considering that incident light propagating from air into glass

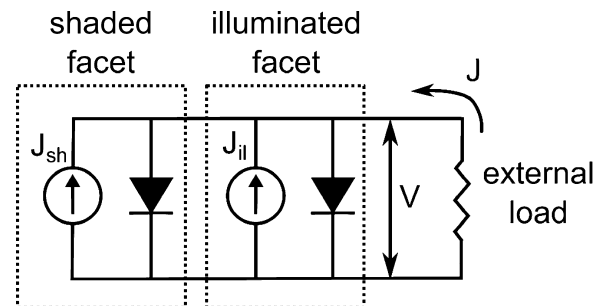


Figure 7 Equivalent circuit of a self-shadowed cell. The shaded and illuminated facets are modeled with the simple one-diode model and are connected in parallel.

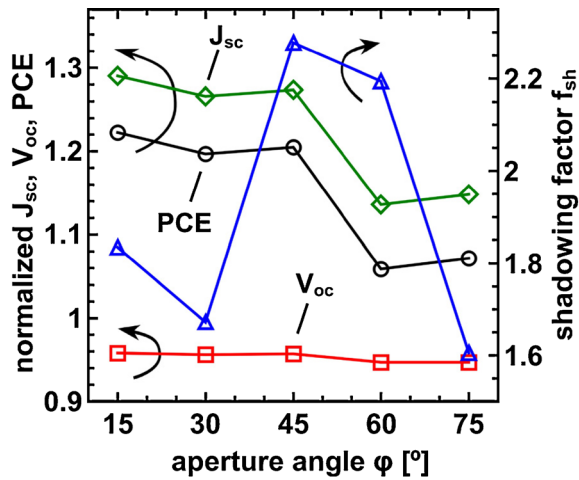


Figure 8 (left axis) Short circuit current J_{sc} , open circuit voltage V_{oc} and power conversion efficiency PCE of structured cells normalized to the planar cell at oblique incidence. (right axis) Shadowing factor f_{sh} defined as the ratio between the photocurrent delivered from the illuminated facet relative to the shaded facet as a function of the aperture angle φ .

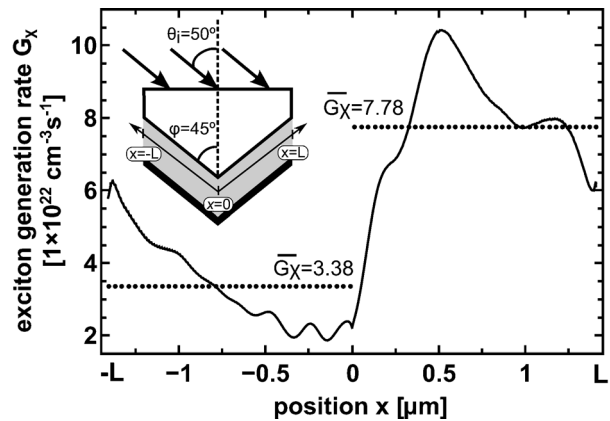


Figure 9 Total exciton generation rate profile along the shaded ($x < 0$) and illuminated facets ($x > 0$) (solid line). The mean values of the exciton generation rate in the shaded and illuminated facets are $\overline{G}_x = 3.38 \times 10^{22} \text{ cm}^{-3} \text{ s}^{-1}$, respectively, and are represented with dotted lines. The inset defines the x -axis and the facet length L .

with $n \cong 1.46$ at $\theta_i = 50^\circ$, refracts with a propagation angle $\theta'_i \cong 32^\circ$. Therefore, for $\varphi = 60^\circ$, Eq. (3) yields $N_{\max} = 1$ implying that every reflected ray in the illuminated facet bounces back to the air. As a result, absorption in the shaded facet is caused mainly by refraction of incoming light [mechanism (i) in Fig. 6], yielding a high f_{sh} . In the case $\varphi = 75^\circ$, partial shadowing occurs because of light impinging at a shallow angle at the shaded facet is weakly absorbed. As φ increases further, the textures becomes flatter approaching the limit of flat surface, *i.e.*, $\varphi = 90^\circ$ (not shown in Fig. 8), where $f_{sh} = 1$.

Importantly, in Fig. 8 we notice that although V_{oc} of all the structured cells is around 5% lower than the planar cell, PCE is up to 22% higher due to the even higher improvement in J_{sc} . This implies that even under partial shadowing due to texturing, textured cells perform better than planar cells also under oblique incidence of light.

Within each facet exciton generation rate is not homogeneous, *i.e.*, a position-dependent generation rate profile is obtained. Figure 9 shows the total exciton generation rate profile in a textured cell with $\varphi = 45^\circ$ at an incidence angle $\theta_i = 50^\circ$ along the shaded ($x < 0$) and illuminated ($x > 0$) facets (solid line). The inset defines the x -axis and the facet length L . The illumination non-uniformity within each facet is not only due to partial shadowing of oblique incident light, since the oscillating patterns suggest that interference plays a role too. In order to study the open circuit voltage drop caused by non-uniform illumination in each facet, we propose a modification to the conventional V_{oc} expression as follows:

$$V_{oc, \text{facet}} = nV_t \ln \left(\zeta \frac{\overline{J_{ph, \text{facet}}}}{J_0} \right) = \overline{V_{oc, \text{facet}}} + nV_t \ln(\zeta_{\text{facet}}), \quad (5)$$

where the photocurrent $\overline{J_{ph, \text{facet}}} = q \overline{G_{x, \text{facet}}} d$, is determined by the mean value of the exciton generation rate $\overline{G_{x, \text{facet}}}$ in each facet (shown in dotted lines in Fig. 9). ζ_{facet} is a statistical factor that accounts for the variations of G_x within each facet, and it is defined as $\zeta_{\text{facet}} = (\overline{G_{x, \text{facet}}} \pm \sigma_{\text{facet}}) / \overline{G_{x, \text{facet}}}$, where σ is the standard deviation of G_x . It turns out that, along each facet, the fluctuation of the photogeneration rate results in local V_{oc} variations of $\pm 15 \text{ mV}$. Since this result was obtained for an incidence angle of 50° , even smaller V_{oc} variations are expected for lower angles corresponding to peak irradiance hours. Therefore, we can rule out any significant variation in the open circuit voltage caused by the illumination inhomogeneity.

4 Conclusions In summary, we have calculated the potential improvement in the photocurrent delivered by CuPc/C₆₀ solar cells deposited on periodic patterned (V-grooves and pyramids) substrates with geometries achievable by current processing technologies, such as DLIP combined with OVPD techniques. The results presented in our work may provide guidelines for designing efficient light trapping geometries.

The overall trend is that light absorption in the active layers is increased by reducing the groove angle (or increasing the geometric aspect ratio). This result is valid for normal as well as oblique radiation incidence. At normal incidence, a V-grooved cell with $1 \mu\text{m}$ period can deliver up to 23% higher photocurrent than planar cells. V-grooved cells with moderate aperture angles of 60° yield 20% higher photocurrent. Larger aperture angles, *i.e.* above 70° , may still show significant light trapping when using submicron periods that trigger diffraction-assisted light trapping.

Even upon self-shadowing of facets occurring at oblique incidence, our full day simulations together with the one-diode electrical model confirm that textured solar cells have a better power conversion efficiency than the planar device, regardless of the aperture of the groove/pyramid.

Acknowledgements This work was supported by CONICET and Universidad Nacional del Comahue (Argentina).

References

- [1] M. A. Green, K. Emery, Y. Hishikawa, W. Warta, and E. D. Dunlop, *Prog. Photovolt. Res. Appl.* **21**, 1 (2013).
- [2] R. Søndergaard, M. Hösel, D. Angmo, T. T. Larsen-Olsen, and F. C. Krebs, *Mater. Today* **15**, 36 (2012).
- [3] F. C. Krebs, S. A. Gevorgyan, and J. Alstrup, *J. Mater. Chem.* **19**, 5442 (2009).
- [4] T. Kirchartz, K. Taretto, and U. Rau, *J. Phys. Chem. C* **113**, 17958 (2009).
- [5] B. P. Rand, J. Genoe, P. Heremans, and J. Poortmans, *Prog. Photovolt. Res. Appl.* **15**, 659 (2007).
- [6] P. Peumans, A. Yakimov, and S. R. Forrest, *J. Appl. Phys.* **93**, 3693 (2003).
- [7] P.-C. Tseng, M.-H. Hsu, M.-A. Tsai, C.-W. Chu, H.-C. Kuo, and P. Yu, *Org. Electron.* **12**, 886 (2011).
- [8] L. Zeng, P. Bermel, Y. Yi, B. A. Alamariu, K. A. Broderick, J. Liu, C. Hong, X. Duan, J. Joannopoulos, and L. C. Kimerling, *Appl. Phys. Lett.* **93**, 221105 (2008).
- [9] J. A. Rand and P. A. Basore, in: *Photovoltaic Specialists Conference, Conference Record of the Twenty Second IEEE*, Vol. 1, Las Vegas, USA, 1991, pp. 192–197.
- [10] H. A. Atwater and A. Polman, *Nature Mater.* **9**, 205 (2010).
- [11] J. Escarré, K. Söderström, M. Despeisse, S. Nicolay, C. Battaglia, G. Bugnon, L. Ding, F. Meillaud, F.-J. Haug, and C. Ballif, *Sol. Energy Mater. Sol. Cells* **98**, 185 (2012).
- [12] K. Yamamoto, A. Nakajima, M. Yoshimi, T. Sawada, S. Fukuda, T. Suezaki, M. Ichikawa, Y. Koi, M. Goto, T. Meguro, T. Matsuda, M. Kondo, T. Sasaki, and Y. Tawada, *Sol. Energy* **77**, 939 (2004).
- [13] J. Springer, B. Rech, W. Retz, J. Müller, and M. Vanecek, *Sol. Energy Mater. Sol. Cells* **85**, 1 (2005).
- [14] J. Meier, J. Spitznagel, U. Kroll, C. Bucher, S. Faÿ, T. Moriarty, and A. Shah, *Thin Solid Films* **451-452**, 518 (2004).
- [15] R. Brendel, A. Gier, M. Mennig, H. Schmidt, and J. H. Werner, *J. Non-Cryst. Solids* **218**, 391 (1997).
- [16] R. Brendel and D. Scholten, *Appl. Phys. A: Mater.* **69**, 201 (1999).
- [17] D. Thorp, P. Campbell, and S. R. Wenham, *Prog. Photovolt. Res. Appl.* **4**, 205 (1996).
- [18] E. Yablonovitch and G. D. Cody, *IEEE Trans. Electron Devices* **29**, 300 (1982).
- [19] M. Berginski, J. Hupkes, M. Schulte, G. Schope, H. Stiebig, B. Rech, and M. Wuttig, *J. Appl. Phys.* **101**, 074903 (2007).
- [20] H. L. Chen, K. T. Huang, C. H. Lin, W. Y. Wang, and W. Fan, *Microelectron. Eng.* **84**, 750 (2007).
- [21] S. Gilles, M. Meier, M. Prömpers, A. van der Hart, C. Kügeler, A. Offenhäuser, and D. Mayer, *Microelectron. Eng.* **86**, 661 (2009).
- [22] R. M. Langford, P. M. Nellen, J. Gierak, and Y. Fu, *MRS Bull.* **32**, 417 (2007).
- [23] A. F. Lasagni, M. Bieda, T. Roch, and D. Langheinrich, *Laser Tech. J.* **8**, 45 (2011).
- [24] A. F. Lasagni, D. F. Acevedo, C. A. Barbero, and F. Mücklich, *Adv. Eng. Mater.* **9**, 99 (2007).
- [25] D. F. Acevedo, G. Martínez, J. T. Arana, E. I. Yslas, F. Mücklich, C. Barbero, and H. J. Salavagione, *J. Phys. Chem. B* **113**, 14661 (2009).
- [26] A. F. Lasagni, P. Shao, J. L. Hendricks, C. M. Shaw, D. C. Martin, and S. Das, *Appl. Surf. Sci.* **256**, 1708 (2010).
- [27] L. Müller-Meskamp, Y. H. Kim, T. Roch, S. Hofmann, R. Scholz, S. Eckardt, K. Leo, and A. F. Lasagni, *Adv. Mater.* **24**, 906 (2012).
- [28] F. Yang, M. Shtein, and S. R. Forrest, *J. Appl. Phys.* **98**, 014906 (2005).
- [29] M. Baldo, M. Deutsch, P. Burrows, H. Gossenberger, M. Gerstenberg, V. Ban, and S. Forrest, *Adv. Mater.* **10**, 1505 (1998).
- [30] R. Brendel, *Prog. Photovolt. Res. Appl.* **3**, 25 (1995).
- [31] V. Andersson, K. Tvingstedt, and O. Inganäs, *J. Appl. Phys.* **103**, 094520 (2008).
- [32] D. Duche, P. Torchio, L. Escoubas, F. Monestier, J.-J. Simon, F. Flory, and G. Mathian, *Sol. Energy Mater. Sol. Cells* **93**, 1377 (2009).
- [33] T. Yagi, Y. Uraoka, and T. Fuyuki, *Sol. Energy Mater. Sol. Cells* **90**, 2647 (2006).
- [34] P. Peumans and S. R. Forrest, *Appl. Phys. Lett.* **79**, 126 (2001).
- [35] J. D. Kotlarski, P. W. M. Blom, L. J. A. Koster, M. Lenes, and L. H. Slooff, *J. Appl. Phys.* **103**, 084502 (2008).
- [36] D. Cheyns, H. Gommans, M. Odijk, J. Poortmans, and P. Heremans, *Sol. Energy Mater. Sol. Cells* **91**, 399 (2007).
- [37] Z. T. Liu, H. S. Kwok, and A. B. Djurisic, *J. Phys. D: Appl. Phys.* **37**, 678 (2004).
- [38] www.comsol.com, COMSOL Group.
- [39] COMSOL AB, *RF Module User's Guide*, COMSOL 3.5a, 2008, Chap. 2.
- [40] J.-M. Jin, *The Finite Element Method in Electromagnetics*, 2nd ed. (Wiley-IEEE Press, New York, 2002), p. 375.
- [41] E. Lorenzo, in: *Handbook of Photovoltaic Science and Engineering*, 2nd ed., edited by A. Luque and S. Hegedus (Wiley, West Sussex 2011.), Chap. 22.
- [42] L. A. A. Pettersson, L. S. Roman, and O. Inganäs, *J. Appl. Phys.* **86**, 487 (1999).
- [43] S.-B. Rim, S. Zhao, S. R. Scully, M. D. McGehee, and P. Peumans, *Appl. Phys. Lett.* **91**, 243501 (2007).
- [44] E. Hecht, *Optics*, 4th ed. (Addison Wesley, San Francisco, 2002), p. 113.
- [45] K. S. Nalwa and S. Chaudhary, *Opt. Express* **18**, 5168 (2010).
- [46] K. Tvingstedt, V. Andersson, F. Zhang, and O. Inganäs, *Appl. Phys. Lett.* **91**, 123514 (2007).
- [47] S. M. Sze and K. K. Ng, *Physics of Semiconductor Devices*, 3rd ed. (Wiley-Interscience, New Jersey, 2006), p. 722.
- [48] M. D. Perez, C. Borek, S. R. Forrest, and M. E. Thompson, *J. Am. Chem. Soc.* **131**, 9281 (2009).